Chapter 13
Applications for Deep Geothermal Engineering

Linmao Xie, Bing Bai, Baotang Shen, Günter Zimmermann, and Ki-Bok Min

Abstract There is mounting interest in developing deep geothermal energy because of its abundant potential as the base-load renewable energy source. Numerical modelling has been widely used to advance the fundamentals towards addressing the grand challenges ahead for efficient and sustainable development of geothermal energy. In this chapter, we first provided a review of state of the art of numerical modelling related to the dynamics of geothermal reservoirs and the stimulation of reservoirs to increase the performance of enhanced geothermal system (EGS). We then presented two modelling applications concerning convective heat transfer through a single fracture and borehole breakout at geothermal wells. The heat transfer characteristics of water flowing through a single fracture within a cylindrical granite specimen was investigated by integrating the experiment and the simulation. The breakout geometry was modeled to estimate the in situ stress at the geothermal sites in Cooper Basin, Australia, and Pohang, South Korea.

Keywords Deep geothermal engineering · Numerical modelling · Enhanced geothermal system (EGS) · Borehole breakout · Heat transfer

---

L. Xie · K.-B. Min (✉)
Department of Energy Resources Engineering, Seoul National University, Seoul, South Korea
e-mail: xielinmao@snu.ac.kr; kbmin@snu.ac.kr

B. Bai
Institute of Rock and Soil Mechanics, Chinese Academy of Sciences (IRSM-CAS), Wuhan, China
e-mail: bai_bing2@126.com

B. Shen
CSIRO Mineral Resources, Brisbane, Queensland, Australia

Shandong University of Science and Technology, Qingdao, China
e-mail: Baotang.Shen@csiro.au

G. Zimmermann
Section 4.8 Geoenergy, German Research Center for Geosciences GFZ, Potsdam, Germany
e-mail: zimm@gfz-potsdam.de

B. Shen et al. (eds.), *Modelling Rock Fracturing Processes*,
https://doi.org/10.1007/978-3-030-35525-8_13

13.1 Deep Geothermal Energy

The geothermal energy, heat in the earth, is a huge source of renewable and clean energy. For example in the US, only 2% of the total thermal energy stored between 3 km and 10 km reservoir is sufficient to provide the US primary energy for 2800 years (MIT 2006). Geothermal energy can be used directly in the form of heat such as the ground source heat pumps (GSHP) or converted to electricity. Ever since the first geothermal electricity production in Larderello, Italy, the human beings have the experience of harnessing the earth heat for electricity generation for more than one century. Geothermal energy can be an attractive option to serve as a CO2-emission-free, base-load renewable energy source (DiPippo 2012).

The total installed capacity from worldwide geothermal power plants increased to 12.7 GW until 2015 and an increase rate of 17% has been achieved in the 5 year term 2010–2015 (Bertani 2016). However, only a small fraction of geothermal energy is currently converted to electricity and geothermal power accounts for only 0.3% of the global electricity supply mainly due to the limited geologically viable locations where the natural heat, water and rock permeability are sufficient for economical heat resource extraction (Van der Hoeven 2013). Except the hydrothermal resources, for the remaining huge amounts of deep geothermal energy, it is stored in the formations that are deficient in water or permeability.

The concept of Enhanced Geothermal System (EGS) has been developed to provide alternative solutions to create technically and economically viable reservoirs, which can loosen the dependency of heat extraction on reservoir natural permeability. In general, the EGS concept involves drilling boreholes to depths where the temperature condition is sufficient for commercial interest and then artificially enhancing or creating the permeability of the reservoir to allow the heat to be extracted efficiently by circulating fluid/steam through injection and production wells. The successful implementation of an EGS system can significantly enlarge the retrievable amount of geothermal resources and these cost-effective ways to mine heat from deep crystalline basement make geothermal energy a worldwide energy contributor regardless of geological limitations.

First attempts to exploit deep geothermal energy by EGS concept should date back to the early 1970s when Los Alamos National Laboratories initiated the Fenton Hill project in USA. This sparks numerous of research and commercial projects in various countries over the past four decades such as Rosemanowe in UK, Soultz in France, Ogachi in Janpan, Basel in Switzerland, Cooper Basin in Australia and Pohang in Korea. General review of the EGS development from its origins to the current state of the art and the projects worldwide is available in Breede et al. (2013) and Olasolo et al. (2016). They highlight the EGS is still on a learning curve and much more efforts are required to make it technologically and commercially viable.

13.2 State of the Art of Numerical Modeling for Geothermal Energy

Numerical modelling in the context of geothermal technology developments and geothermal energy in general aims at different targets. In the first place, it is related to the understanding of the dynamics of geothermal reservoirs, to describe the reservoir properties and to study time dependent processes (e.g. Diersch 2013; Kolditz et al. 2015). The second topic is related to the stimulation of reservoirs to increase the performance of the reservoir systems in context with enhanced geothermal systems (EGS). In most cases these stimulations are based on acidizing/chemical procedures (Portier et al. 2009), thermal effects (Charlez et al. 1996) and on different kinds of hydraulic fracturing treatments (e.g. Economides and Nolte 2000). Further modelling approaches are related to process engineering and power plant design (e.g. Frick et al. 2010) to convert heat to electricity.

Various physical and chemical processes need to be addressed in geothermal modelling based on the complexity of the problem to be solved. Since heat in place is one of the main principle targets, the temperature field needs to be evaluated to model conductive and advective heat flow scenarios. This can be on basin or regional scale (Scheck-Wenderoth et al. 2014; Freymark et al. 2017) to explore the sources and potential for geothermal heat and on reservoir scale to estimate and quantify the life cycle of geothermal heat extraction. In the latter case this modelling is in most cases coupled to fluid flow to describe the hydraulic behavior of geothermal reservoirs in terms of productivity and injectivity and to multi-phase flow to address gas migration.

Pruess (2006) presented a simulation of an EGS system using CO2 as circulation fluid and has modelled it with TOUGH2 for a five spot configuration. A similar study was carried out by Luo et al. (2014) using the conditions of the EGS site in Groß Schönebeck (Zimmermann & Reinicke 2010; Zimmermann et al. 2010). They used the software FLUENT for simulating fluid flow and heat transfer, a well-established CFD (computational fluid dynamics) software package. It uses the finite-volume method to solve the Navier-Stokes equations.

The open source finite element based code OpenGeoSys (OGS, e.g. Kolditz et al. (2015)) has been used in a variety of geothermal sites for numerical modelling of the dynamic behavior of geothermal reservoirs. Cacace et al. (2013) modelled a fractured carbonate reservoir in the Molasse Basin, Germany, to estimate the potential for geothermal heat extraction. OGS is capable of calculating fluid flow and heat transport through a porous media, which may be intersected by a network of discrete fractures with arbitrary shape (Blöcher et al. 2010). Fluid flow through fractures is calculated using the cubic law assuming laminar flow between smooth parallel plates. A detailed description of the governing equations and numerical schemes are given in Watanabe et al. (2010) and Watanabe et al. (2012).

In case of chemical stimulation, like acidizing the reservoir rocks to enhance productivity or injectivity, the modelling includes a chemical coupling in addition. Chemical investigations aim at understanding mineral solution/dissolution. This is related to precipitation of minerals from formation water in context with temperature changes during production and circulation, alterations of mineral phases and gas-dissolution and -exsolution.

Regenspurg et al. (2018) studied the impact of drilling mud on chemistry and microbiology of an exploration well for aquifer thermal energy storage (ATES) in Berlin (Germany). Mineral saturation indices were determined by the PhreeqC code (Parkhurst and Appelo 2013).

A further type of coupling to model the properties and dynamics of geothermal reservoirs is related to rock mechanics and fracture mechanics. It can be applied to stress changes in context with plate tectonics representing long time scales or short-term stress changes due to hydraulic stimulation treatments. These modelling approaches include linear elastic (stress) problems, brittle deformation, fracturing in tensile and shearing mode and poromechanics to study pore pressure diffusion in geothermal reservoirs. In the latter, compaction, poro-elasticity, plasticity and thermo-elasticity are addressed to study static and dynamic problems.

To evaluate the thermal, hydraulic and mechanical response due to a waterfrac stimulation treatment (Zimmermann et al. 2010) and due to a projected 30 Years production and injection period at the geothermal research well GtGrSk4/05 in Groß Schönebeck, Germany, a numerical investigation of the reservoir has been carried out. This investigation relies on modeling implicitly coupled and non-linear thermal–hydraulic–and mechanical processes within the fractured porous reservoir. Cacace and Jacquey (2017) applied the GOLEM simulator that builds on the flexible, object oriented MOOSE framework (Gaston et al. 2009). Similar to the OpenGeoSys code described above, fractures are considered as being of lower dimension (2D structures) than the hosting deformable 3D porous rock and their hydraulic aperture is then used as scaling parameter to ensure continuous exchange of fluid mass and energy within the fracture–solid matrix system (Cacace and Jacquey 2017).

The study by Rutqvist et al. (2015) used coupled thermal, hydraulic and mechanical (THM) models to investigate injection strategies at the Northwest Geysers Enhanced Geothermal System (EGS) Demonstration Project, California, and to predict the corresponding extent of the stimulated volume. The analysis was performed with the TOUGH-FLAC simulator (Rutqvist 2011), which is capable of modeling multiphase flow within the steam-dominated geothermal system at The Geysers.

Several commercial hydraulic fracturing modelling tools to predict and evaluate the success of stimulation treatments in geothermal reservoirs exist, which are in most cases adapted from the hydrocarbon industry (e.g. Warpinski et al. 1994). At the Groß Schönebeck site, the 3D fracturing code FRACPRO (Cleary 1994) was used to determine expected properties like well head pressure and dimensions of the generated fractures and using the treatment data thereafter to obtain the achieved fracture geometry based on the model results (Zimmermann et al. 2010). Theoretical background of the mechanics of hydraulic fracturing are available at, e.g., Yew (1997), Economides and Nolte (2000) and Guéguen and Boutéca (2004).

The potential for enhanced geothermal systems in Alberta, Canada, were modelled in four potential target formations with the fracturing simulator MFrac (MFRAC 2011), which is formulated between a pseudo-3D and a full 3D model (Hofmann et al. 2014b). For decades, this software has been routinely used to model hydraulic fracturing treatments for application in the hydrocarbon industry (e.g. Warpinski et al. 1994). Another study of Hofmann et al. (2014a) performed process simulation for different hydraulic fracturing scenarios to investigate the potential for hot water generation for oil sands processing from enhanced geothermal systems (EGS).

The two dimensional version of the discrete element model Particle Flow Code (PFC2D, Itasca (2008) was used to simulate a complex fracture development in low permeable granitic rocks based on the properties of the Soultz-sous-Forêt geothermal site (Yoon et al. 2014). The model consists of discrete non-deformable cylindrical particles with unit thickness which are connected at their contact points by parallel bonds of finite strength. According to the Mohr-Coulomb criterion they may fail in tensile mode (Mode I failure) and in shear mode (Mode II failure) (details in Potyondy and Cundall 2004). For the simulation of hydraulic stimulation treatments, a fluid flow algorithm and an explicit hydro-mechanical coupling scheme are used (Yoon et al. 2014).

Zang et al. (2013) used PFC for a modeling and experimental study to simulate a cyclic mechanical and cyclic hydraulic fracturing treatment, resulting in a lower seismicity and a reduction of the number of events if compared to a conventional protocol. They argued that the loading cycles fatigues the rock by frequent lowering of the crack tip stresses. The detailed description of the concept of fatigue hydraulic fracturing and its geothermal application is discussed in Zang et al. (2017, 2018). Similar studies with a more sophisticated geometry to simulate a multi-stage fracturing design (Yoon et al. 2015a), the stress shadowing effect (Yoon et al. 2015b) and the presence of a nearby fault (Yoon et al. 2015c) confirm the findings of Zang et al. (2013).

The simulation environment TRNSYS (Klein 1976; Beckman et al. 1994) is used for power plant design and process engineering and is based on thermodynamic principles to perform comprehensive life cycle analyses (Frick et al. 2010) and to quantify the characteristics of aquifer thermal energy storage (ATES) systems utilized for cooling buildings (Kranz and Frick 2013).

13.3 Convective Heat Transfer Through a Single Fracture

13.3.1 Introduction

A thorough understanding of convective heat transfer between the rock fracture and the circulating fluid plays a key role in EGS geothermal recovery (Huang et al. 2016;

Xu et al. 2015). The heat transfer process between the fluid and the fracture wall is influenced by many factors such as the composition of the fluid, the geometry of the rock surface, the mineral composition of the rock, the roughness of the fracture and the hydrodynamics of the fluid motion that past the surface (Tsang 1984; Zhang et al. 2015; Zhao 2014). For this complex issue of convective heat transfer, although widely studied, it is still not fully understood even for the case of a single rock fracture. The heat transfer coefficient is a widely used index to characterize the heat transfer properties of the different parts of a fracture and this can be described by local heat transfer coefficient (LHTC). However, the LHTC of a single rock fracture is scarcely mentioned in literature. This section is to investigate the heat transfer characteristics of water flowing through a single fracture within a cylindrical granite specimen under confining pressures by combining experimental and numerical simulation results (Bai et al. 2016; He et al. 2016).

13.3.2 Methodology

13.3.2.1 Experimental

The tests were implemented on the conventional triaxial test platform with the function of heating, and the test schematic diagram is shown in Fig. 13.1. In each test, a given temperature is set all the same at the outside surface of the fractured rock

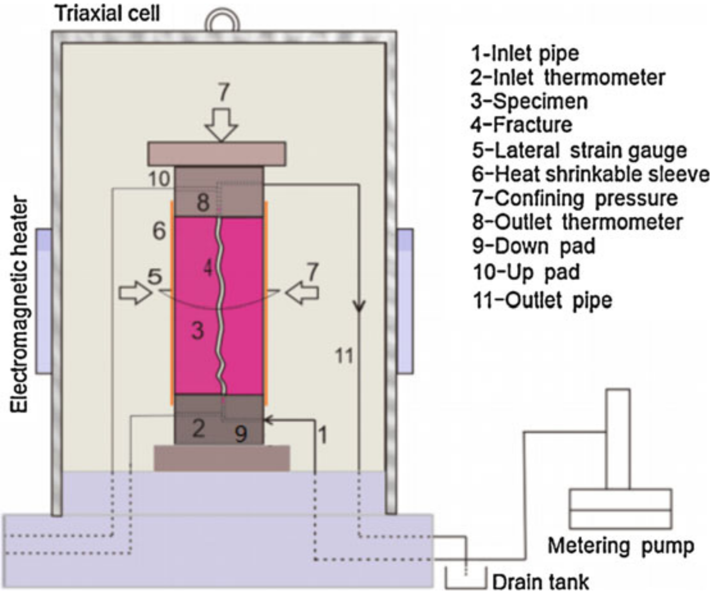

Fig. 13.1 Experimental schematic diagram

Table 13.1 Physical properties of the rock (r) and water (w)

Density		Specific heat capacity		Thermal conductivity	
ρ_r (kg/m^3)	ρ_w (kg/m^3)	$C_{p,r}$ (J/kg·K)	$C_{p,w}$ (J/kg·K)	K_r (W/(m·K))	K_w (W/(m·K))
2200	1000	880	4200	2.78	0.662

cylinder. Along the longitudinal direction, water flows in at a preset flow rate from one side of the fracture and flows out at the other. During this process, heat exchange takes place between the water and the fracture walls of the two halves of the rock specimen. The water temperatures at both inlet and outlet of the fracture are obtained by direct measurement.

The basic physical properties of the rock specimen and water used in the experiment are listed in Table 13.1, which will be the input parameters in the subsequent simulations.

In this study, the local heat transfer coefficient will be implemented as the overall heat transfer coefficient at a very small piece of the fracture with its definition given in Eq. (13.1). LHTC values can be calculated at each discretized element by Eq. (13.1) with the corresponding fluid temperature, velocity, and the inner wall temperature from the numerical simulations.

$$h' = \frac{c_{p.w}\rho_w u\delta(T_2 - T_1)}{2(\mathrm{x}_2 - \mathrm{x}_1)\left(T_i - \frac{T+T_2}{2}\right)} \tag{13.1}$$

where h' is the local heat transfer coefficient, $c_{p,w}$ is the specific heat capacity of water at constant pressure, ρ_w is the density of water, u is the steady flow velocity of water, δ is the aperture length, T_2 and T_1 are the temperatures of two adjacent points of the water along the flow direction and x_2-x_1 are the x-coordinates of the two points, respectively, T_i is the inner surface temperature of the rock sample.

13.3.2.2 Numerical Modeling Method

A two-dimensional numerical model was developed on the Comsol Multiphysics simulator (Comsol Multiphysics 2018). In subsequent simulations, the actual geometry was built with the profile obtained by hypothetically cutting the specimen with a plane passing through the section center and perpendicular to the normal of the fracture surface (Fig. 13.2a), and the picture of the fracture wall was rebuilt from the laser scanning result of the granite specimen (Fig. 13.2b).

Figure 13.3 shows the conceptual geometry where the physical and numerical model of the coupled flow and heat transfer is defined.

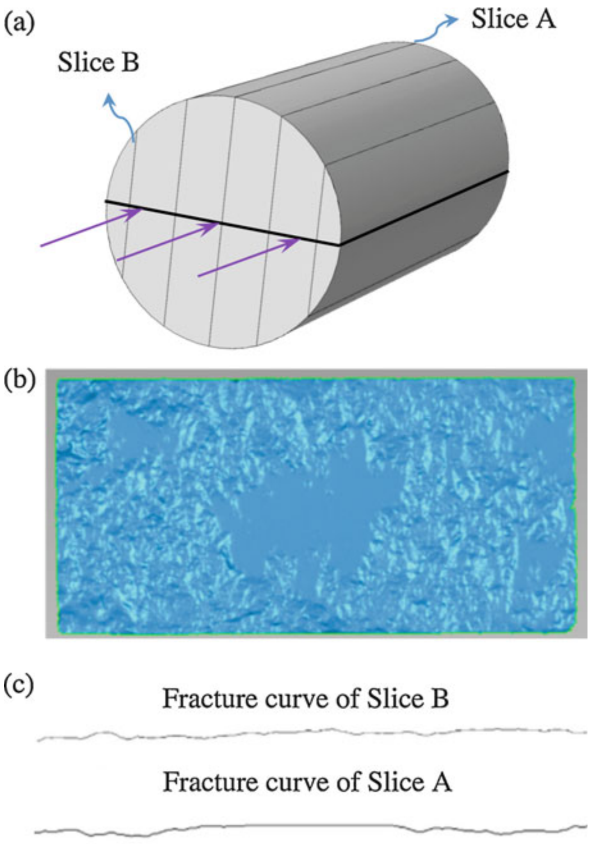

Fig. 13.2 Model geometrical configuration. (**a**) 2D profiles of specimen in the simulations, (**b**) the morphology of the rock fracture surface and (**c**) the fracture curves corresponding to Slice A and Slice B, respectively

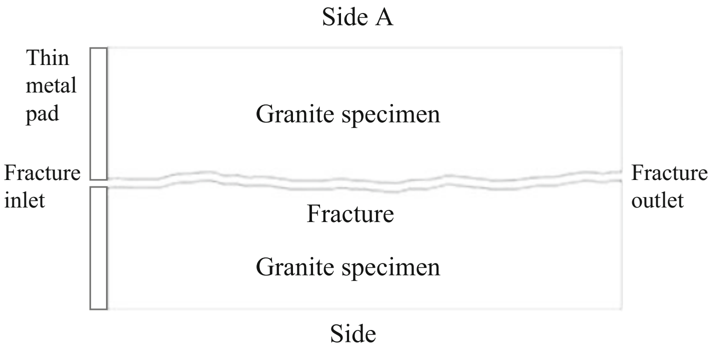

Fig. 13.3 2D model based on the slice geometry

The single-phase water flow in the fracture follows the Navier-Stokes equations, which read,

$$\nabla \cdot \mathbf{u} = 0 \tag{13.2}$$

$$\rho_w \frac{\partial \mathbf{u}}{\partial t} + \rho_w \mathbf{u} \cdot \nabla \mathbf{u} = -\nabla p + \nabla \cdot \left(\mu \left(\nabla \mathbf{u} + (\nabla \mathbf{u})^T \right) - \frac{2}{3} \mu (\nabla \cdot \mathbf{u}) I \right) \tag{13.3}$$

$$\begin{aligned} \rho_w C_{p,w} \left(\frac{\partial T_w}{\partial t} + (\mathbf{u} \cdot \nabla) T_w \right) &= -\nabla \cdot \mathbf{q_w} + \tau \\ &: S - \frac{T_w}{\rho_w} \frac{\partial \rho_w}{\partial T_w} \left(\frac{\partial p}{\partial t} + (\mathbf{u} \cdot \nabla) p \right) \end{aligned} \tag{13.4}$$

where ρ_w is the water density (kg/m^3), $\mathbf{u}$ is the velocity vector (m/s), p is pressure (Pa), τ is the viscous stress tensor (Pa), $c_{p,\ w}$ is the specific heat capacity at constant pressure (J/(kg·K)), T_w is the absolute temperature (K), $\mathbf{q_w}$is the heat flux vector in water (W/m^2), and $\boldsymbol{S}$ is the strain-rate tensor.

Eqs. (13.2)–(13.4) are continuity equation, momentum conservation equation and energy conservation equation, respectively. With a constant water density, the heat energy equation of water is simplified as

$$\rho_w C_{p,w} \left(\frac{\partial T_w}{\partial t} + (\mathbf{u} \cdot \nabla) T_w \right) = -\nabla \cdot \mathbf{q_w} \tag{13.5}$$

The heat conduction equation in the granite specimen is

$$\rho_r C_{p,r} \frac{\partial T_r}{\partial t} = -\nabla \cdot q_r \tag{13.6}$$

where q_{r} is the heat flux vector in granite specimen (W/m^2).

Proper boundary and initial conditions are required to solve the equation system. At the inlet of the fracture, the flow equation of water is set to a constant flow rate boundary, while the heat energy Eq. (13.4) is set to a boundary of a given temperature measured in the experiment. At the outlet of the fracture, flow Eq. (13.3) is set to atmospheric pressure which is a given pressure boundary. The initial temperature of the fracture water is set to the same as the initial temperature of the rock specimen. On the outside boundaries A and B (Fig. 13.3), the temperatures are, respectively, set to a given temperature, the same as the temperature of the oil in the triaxial cell. The initial temperature inside the rock is also set to the same temperature as the oil.

According to the experimental schematic diagram in Fig. 13.1, two metal pads are placed together with the rock specimen. The upper face of the up pad contacts directly with the hydraulic oil, and its boundary is relatively easier to determine than the boundary of the down pad that is connected with the whole base of the pressure chamber. It would be easier to deal with the boundaries if both of the end pads and the entire chamber base were included in the numerical model, but much more complexity would be introduced into the model geometry. To avoid the complexity, proper boundary conditions are needed to be set at both the inlet and outlet ends of the specimen. The outlet side of the specimen was found to be very close to an adiabatic boundary, possibly for two reasons. The first possible reason is the unavoidable minute gap between the specimen and the outlet pad. The second possible reason is that the temperature of the water is very close to the specimen after it reaches the outlet side and hence has a very weak effect on the outlet boundary. However, at the inlet side, the temperature of water is much lower than the temperature of the specimen and the oil, and this variation will lead to a non-uniform temperature distribution on the inlet side of the specimen. As this temperature distribution is unknown, it is not possible to set a given temperature boundary there. Furthermore, an adiabatic boundary is also not reasonable. When an iron layer with a thickness (80 mm used in the simulations) greater than a certain value (approximately 3 mm in our case) is added to the inlet side of the specimen, well-matched results can be achieved if a uniform temperature is specified on the metal boundary condition. At the same time, further increase of the thickness of the metal layer was found to have no effect on the results.

13.3.3 Results and Discussion

13.3.3.1 Numerical Results and Verification

Nine simulation cases with different fracture apertures and different flow rates were conducted. Table 13.1 lists some of the simulation parameters and they are identical with experimental measurements. The confining temperature was 90 °C. As the water temperatures at the outlet of the fracture are not assigned, their calculated values can be indicators of the correctness of the numerical model.

The distributions of flow field and temperature field can be important indicators to judge the rationality of the numerical results. Considering the space limitation, we show only 3 cases of the pressure and temperature field without loss of representation in Fig. 13.4. It can be seen that the simulated results in these figures are in complete agreement with our rational expectations. Therefore, it can be concluded that the numerical model we developed produced reasonable simulation results.

All the simulation values and test values of the water temperature at the outlet together with their relative deviations are shown in Fig. 13.5. Most of the simulation results and their corresponding experimental values are in very good agreement since the maximum relative deviation is only 2.1%. This agreement proves that the numerical model was developed properly.

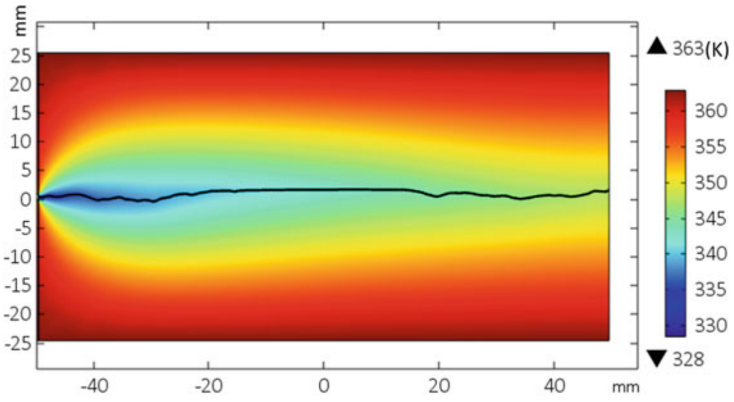

a) 30ml/min, 125μm, 900s

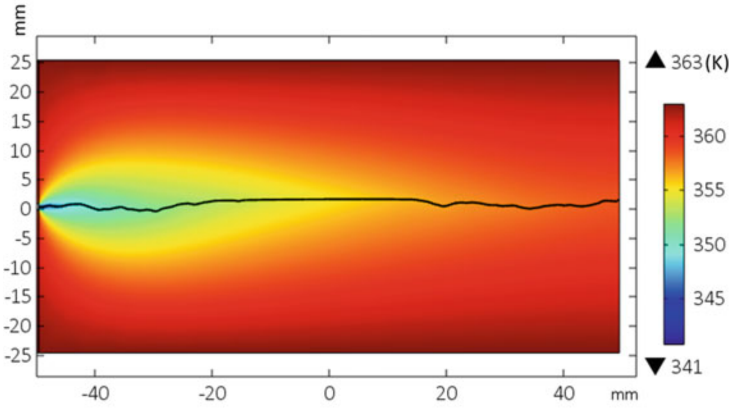

b) 15ml/min, 95μm, 900s

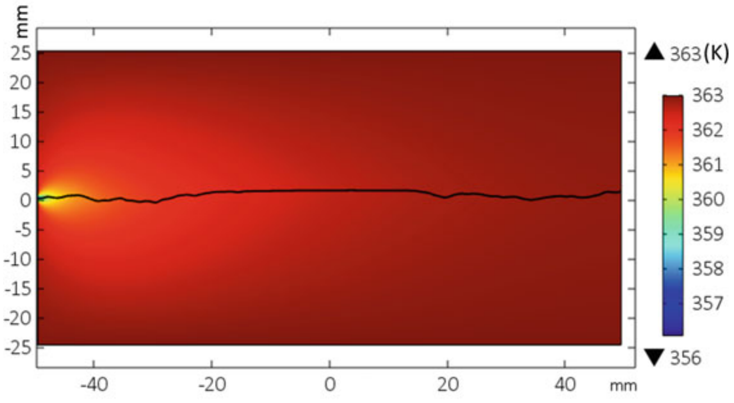

c) 5ml/min, 80.5μm, 900s

Fig. 13.4 Temperature distribution in both the fracture water and the specimen

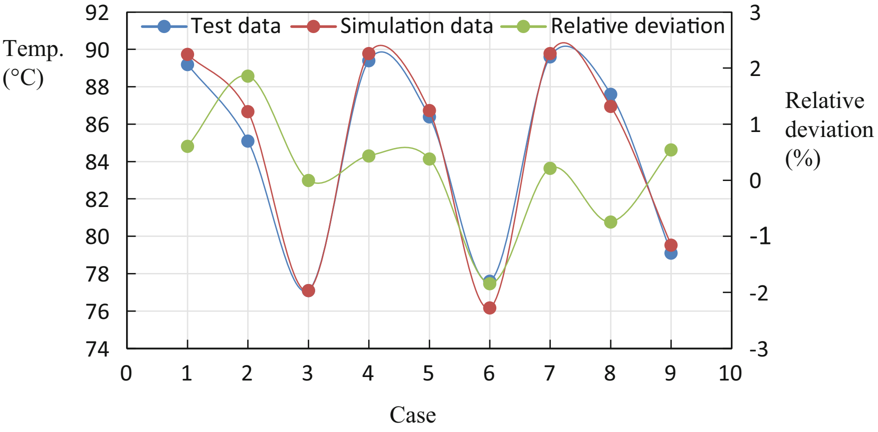

Fig. 13.5 Water temperature at the outlet from simulations and experiments, and their relative deviation

13.3.3.2 Local Heat Transfer Characteristics

Figure 13.6 shows the distribution of the local heat transfer coefficients at different flow rates. (Fracture aperture: 95 μm). Fig. 13.6a corresponds to the slice A and Fig. 13.6b corresponds to slice B. For a fixed flow rate, the LHTC is different everywhere. This means that the LHTC is closely related to the fluctuation of the fracture morphology. Moreover, at a given position, the flow rate does not significantly affect the local heat transfer capacity. On the other hand, the fracture aperture has more effect on LHTC. Fig. 13.7 shows that narrower fracture produced larger LTHCs Fig. 13.7a corresponds to the slice A and Fig. 13.7b corresponds to slice B.

In Fig. 13.6b, the LHTC is relatively lower and uniform in the flat part of the fracture. However, in the rougher regions near the specimen ends, there are some sharp changes. This means that the roughness of the fracture will notably affect the LHTC. This is more clearly shown in Fig. 13.8 which presents the comparison of waviness and LHTC. In Fig. 13.8, the local waviness is characterized with the altitude of the corresponding point at the fracture surface. From this figure, we can see that larger waviness corresponds to less LHTC value and the sunken positions at the fracture surface have much larger LHTC. The comparison of the LHTC distributions with five different fractures shows that there is always a negative correlation between the fracture waviness and the LHTC. Overall, the LHTC distribution mainly depends on the fracture surface roughness, followed by fracture aperture and flow rate. However, surface roughness has little effects on the water temperature and temperature distributions of the inner surface. That is to say, the surface roughness influences the flow rate along the flow direction, thus affecting the LHTC distributions.

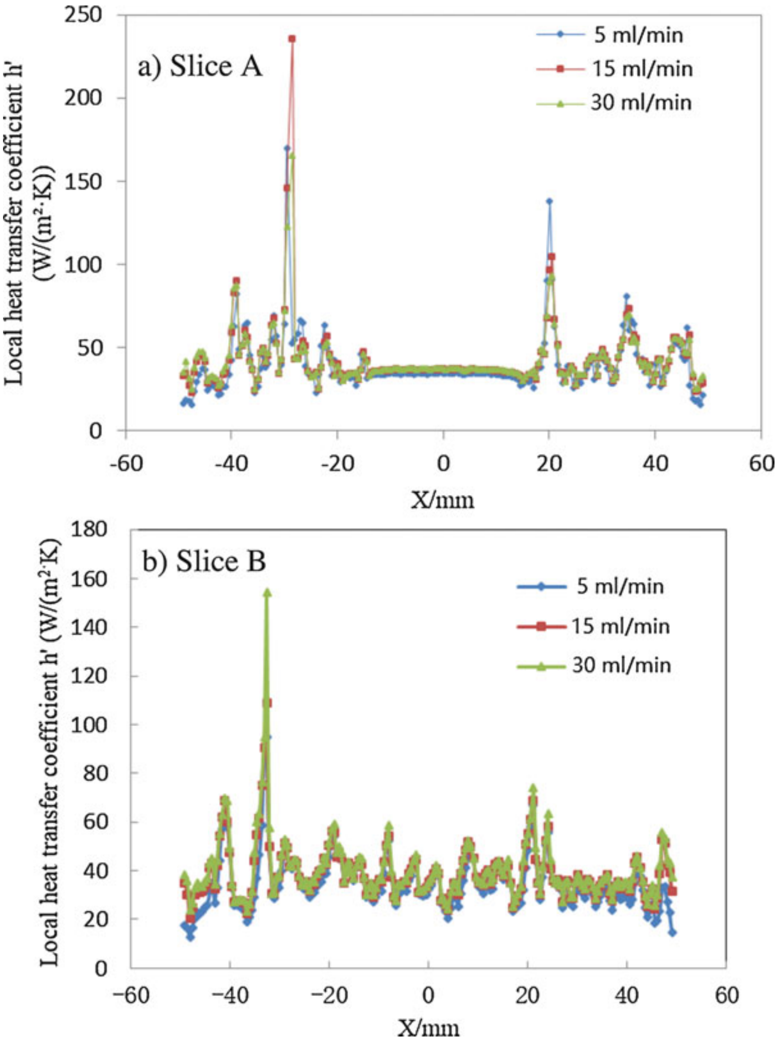

Fig. 13.6 Distribution of LHTCs under different flow rates (fracture aperture = 95 μm)

13.4 Borehole Breakouts and In Situ Stress Estimation

13.4.1 Background

Estimating the state of field stress is a fundamental issue for geothermal energy development which involves many geomechanical processes. The in situ stress information, including orientation and magnitudes, is the basic input for operation design and interpretation.

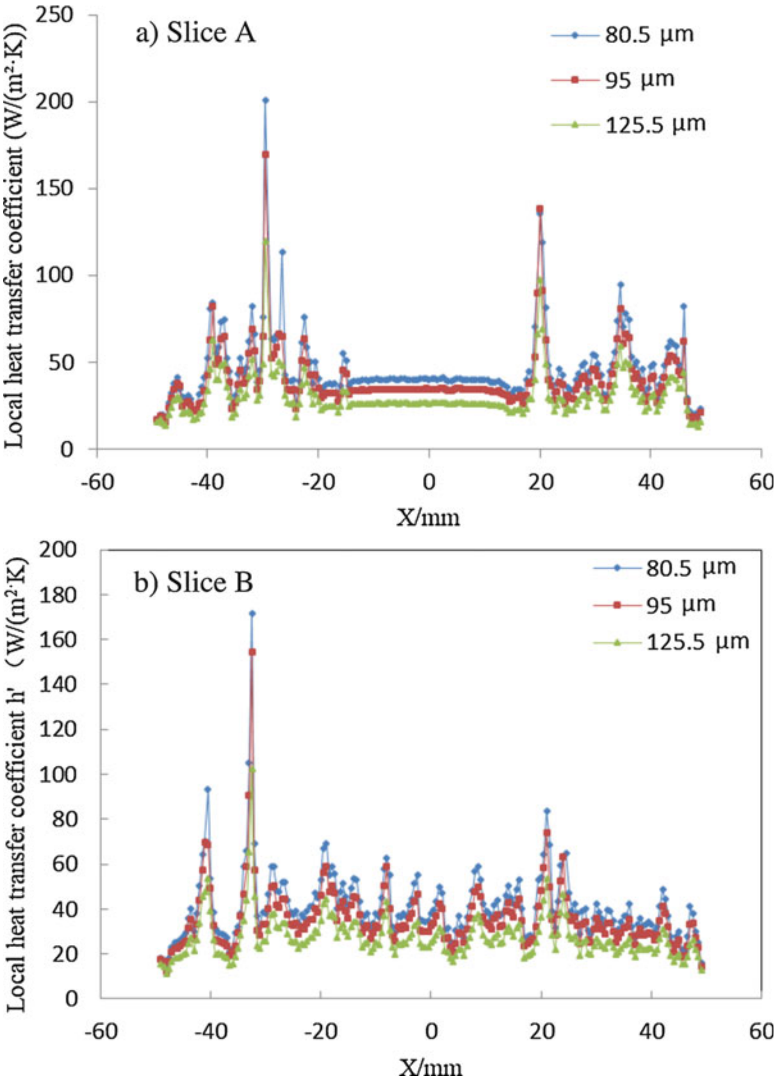

Fig. 13.7 Distribution of LHTCs for different fracture apertures (Flow rate of 5 ml/min)

The long term borehole stability is necessary for extracting the geothermal resources. At a great depth of several kilometres, the borehole is subjected to high stress concentration and sufficient strong casing and cementing are required to prevent borehole failure during the project lifespan. The good knowledge of field stress regimes is critically important for the appropriate casing and cementing design.

The hydraulic stimulation is commonly used for enhancing or creating the permeability of heat exchange reservoir. The hydrofracturing and hydroshearing

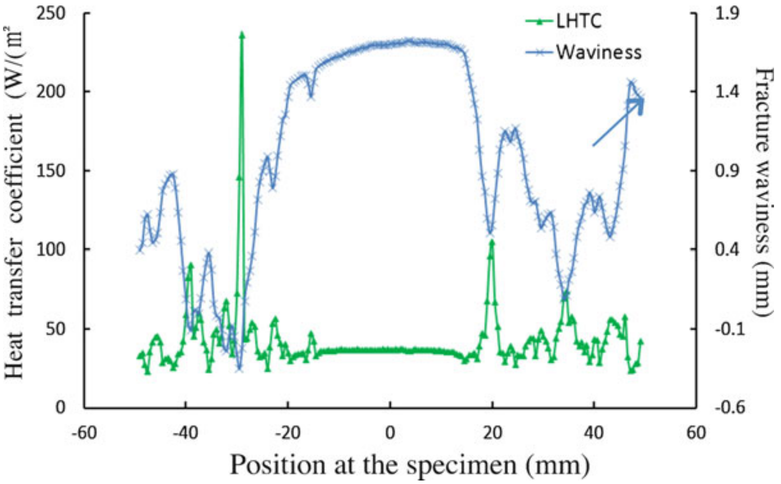

Fig. 13.8 comparison of waviness and LHTC (test case: flow rate = 15 mL/min; fracture aperture = 95 μm)

are two major mechanisms accounting for permeability generation. The pressure required for initiating a hydraulic fracture is directly controlled by the stress magnitude and the fracture propagates perpendicular to the minimum principal stress. As for the evolution of shearing of natural fractures, it is basically governed by the fracture orientation and field stress. Increasing concern has been raised for the induced seismicity associated with the hydraulic stimulation and the big seismic events can even lead to a permanent closure of a project (Häring et al. 2008). The field stress determination is desperately required because the in situ stress plays a significant role in the interpretation, management and mitigation of induced seismicity.

Since the geothermal reservoir is often at a great depth of several kilometres, direct measurement of the in situ stresses by the conventional methods such as hydraulic fracturing is very difficult. The application of core-based methods of stress measurement is limited because of high technical difficulties and financial costs for deep core recovery.

Borehole breakout commonly occurs at such depths and it is usually observed by borehole televiewer logging and caliper logging. As the breakout happens at the azimuth of the minimum horizontal stress, it is a reliable indicator of the stress orientation. In addition, breakout dimensions (the depth and angular width of breakout, as shown in Fig. 13.9) store information on in situ stress magnitudes. The inversion of breakout geometry can be used to estimate stress magnitudes, however, there are more uncertainties because of its dependence on rock properties and failure criteria.

Borehole breakout analysis has been routinely used for estimating deep in situ stresses (Zang and Stephansson 2009). Numerous examples of field application exist in the contexts of deep continental drilling programs such as KTB, Germany (Vernik

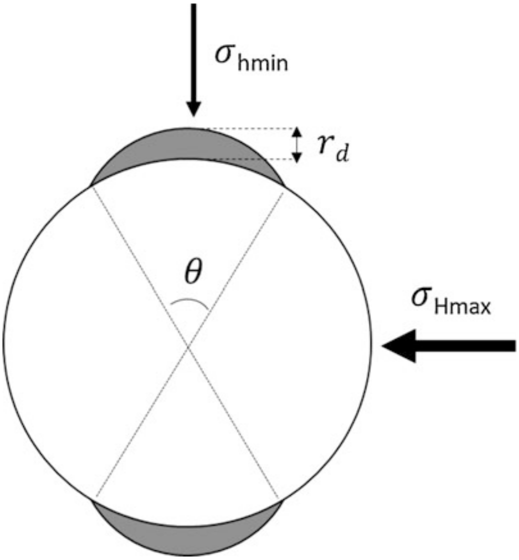

Fig. 13.9 Schematic of borehole breakout in the direction of minimum horizontal stress. Breakout dimensions include breakout depth (r_d) and breakout width (θ)

et al. 1992), hydrocarbon exploitation development such as the GBRN Pathfinder well in Gulf of Mexico, USA (Zoback and Peska 1995) and deep geothermal energy development such as Soultz EGS site (Valley and Evans 2007).

Considering the uncertainties of rock properties and the difficulties of retrieving complete and reliable breakout data in harsh conditions, breakout analysis is often combined with other available stress measurement methods, as suggested by the integrated stress estimation strategy.

Numerical modelling can provide complementary insights for borehole breakout analysis. Especially the appropriate numerical inversion that accounts for the progressive failure of rock until the forming of final breakout geometry benefits the interpretation of stress magnitudes.

The fracture propagation code FRACOD developed by Shen and Stephansson (1994) and FRACOM (2002) has been shown to effectively simulate the breakout process (Shen et al. 2002). It is a 2D boundary element code with the F criterion of fracture propagation and it can realistically simulate the actual process and mechanism of borehole breakouts by simultaneous consideration of mode I, mode II and mixed mode failure. Borehole breakouts are predicted numerically in the following steps: (1) Setting up the numerical model including defining borehole geometry, rock properties and in situ stresses; (2) FRACOD automatically calculates stresses in the borehole walls using solid mechanics principles; (3) FRACOD then determines if any failure (fracture initiation) occurs in the borehole wall based on the stresses obtained and the rock strength; (4) If failure is detected to occur, new fractures will be generated in the model and FRACOD then determines if and how they propagate; (5) Breakouts will be formed when fractures in the borehole wall propagate and coalesce; (6) The dimensions of the final breakouts are obtained when there is no further failure and fracture propagation in the borehole wall.

FRACOD was used in this study to predict the breakout dimensions under various stress combinations. FRACOD is a 2D code, and only horizontal planes (perpendicular to the wellbore axis) are considered. The study is aimed at estimating the magnitude of the horizontal stresses only. The vertical stress is commonly assumed to be the gravity load determined from the cover depth and the rock density.

We present two examples for illustrating the stress magnitude estimation based on the modellings of breakout geometries by FRACOD. The first one is the back analysis of horizontal stress magnitudes of Cooper Basin geothermal site in Australia based on the correlations among modelled breakout dimensions, stress and rock strength (Shen 2008). A second one involves the determination of σ_{Hmax} magnitude of Pohang geothermal site in Korea (Kim et al. 2017) in which the breakout modelling was part of the integrated stress estimation and the magnitude of σ_{hmin} was provided by hydraulic fracturing method with relatively high certainty.

13.4.2 Application to Cooper Basin Geothermal Site, Australia

This study focuses on the Habanero No. 1 well which was drilled by Geodynamics Ltd. at Cooper Basin (Shen 2008). It was the first deep well drilled for developing hot fractured rock (HFR) geothermal resource in Australia. The well was drilled to a depth of 4421 m with bottom hole temperature of 240 °C. Extensive borehole breakouts occurred in the granite section (depth = 3650–4421 m) of Habanero No. 1 well after drilling. The direction and dimension of borehole breakouts were measured using borehole geophysical logging.

The study was conducted in the following steps:

- Establish a quantitative relation between breakout dimensions and in situ stresses in granitic rock by means of numerical modelling.
- Back-calculate the in situ stresses using the measured borehole breakout data at Habanero No. 1 well at various depths.
- Evaluate the overall stress state and stress ratios in Habanero No. 1 well granite.

13.4.2.1 Input Properties

The mechanical properties required in this study include the intact rock strength, fracture contact properties and fracture toughness. Due to the lack of directly measured data of the Habanero No. 1 granite, the mechanical properties used in this study are mostly based on previous modelling experience for granitic rock properties (Stephansson et al. 2003). Some modifications of the data were made after limited sensitivity studies to reproduce the breakout shape observed in the AECL experimental tunnel (Martin et al. 1997). The values of the mechanical properties used in this study are listed in Table 13.2.

Table 13.2 Summary of mechanical properties used in the model

Mechanical properties	
Intact rock strength:	
Young's modulus	65 GPa
Poisson's ratio	0.25
Cohesion	31 MPa
Friction angle	35°
Uniaxial compression strength (σ_c)	120 MPa
Fracture toughness:	
Mode I toughness	1.35 MPa $m^{1/2}$
Mode II toughness	3.07 MPa $m^{1/2}$
Joint/fracture properties:	
Normal stiffness Kn	50,000 GPa/m
Shear stiffness Ks	12,550 GPa/m
Friction angle	25.5°
Cohesion	0
Dilation angle	2°

The fracture properties are found to have minor effects on the results once they are fallen into a range (i.e. the stiffness values are high enough and the friction angle is low enough). The chosen values in Table 13.2 are considered to be reasonable based on the previous modelling experience in granite at Tono Mine in Japan and the diorite at Äspö Hard Rock Laboratory in Sweden.

13.4.2.2 Modelling Results

Fifteen cases with different combinations of the major and minor principal horizontal stresses (σ_{Hmax} and σ_{hmin}) were simulated (Table 13.3). The modelled magnitude of σ_{Hmax} and σ_{hmin} varies in the range of 50–80 MPa and 10–60 MPa, respectively. The stress ratio $\sigma_{Hmax}/\sigma_{hmin}$ varies in the range of 1.2–8.0. Note that the stresses used in the numerical modelling are effective stresses and pore pressure is excluded at this stage.

Figure 13.10 shows a typical set of the modelling results.Several observations can be made based on the modelling results:

- For a given σ_{Hmax}, a lower σ_{hmin} is found to result in a deeper breakout. Because the variation of σ_{hmin} affects the stress ratio $\sigma_{Hmax}/\sigma_{hmin}$ much more severely than an overall average stress (for example $(\sigma_{Hmax} + \sigma_{hmin})/2$), it implies that the depth of the breakout is very much dependent on the stress ratio $\sigma_{Hmax}/\sigma_{hmin}$, rather than an average stress index.
- For a given σ_{hmin}, a higher σ_{Hmax} will result in a wider breakout, implying that the width (or azimuth angle) of the breakouts depends on the magnitude of the major horizontal principal stress.

Table 13.3 Summary of modelling results

No.	σ_{Hmax} (MPa)	σ_{hmin} (MPa)	$\sigma_{Hmax}/\sigma_{hmin}$	Breakout angle (°)	Normalised breakout depth (% of borehole radius)
1	80	60	1.33	117	28%
2	80	40	2	90	31%
3	80	25	3.2	81	37%
4	80	10	8	72	32%
5	70	50	1.4	86.4	24%
6	70	30	2.33	72	24%
7	70	15	4.67	72	26%
8	60	50	1.2	64.8	16%
9	60	40	1.5	57.6	14%
10	60	30	2	57.6	26%
11	60	20	3	64.8	20%
12	60	10	6	57.6	29%
13	50	30	1.67	14.4	5%
14	50	20	2.5	36	20%
15	50	10	5	43.2	24%

- Breakouts are caused by combined tensile and shear fracturing. The initial fracturing starts at the borehole wall and propagates into the rock. Some failures also initiate inside the borehole wall during breakout development.

Note that the results for some cases are off the trend, due to the randomness in the fracture initiation and propagation process.

13.4.2.3 Correlations Between Stress/Strength Ratio and Breakout Angle

For a perfect borehole without fracturing, the tangential stress at the borehole wall can be determined using elasticity theory. The azimuth angle within which the tangential stress exceeds the uniaxial compressive strength can be calculated from Eq. (13.7).

$$\frac{1-(\sigma_{H\max}+\sigma_{h\min})/\sigma_c}{2(\sigma_{H\max}-\sigma_{h\min})/\sigma_c}=\cos(\theta) \tag{13.7}$$

Where

θ = breakout angle at the borehole wall (°)
σ_c = uniaxial compressive strength of rock (MPa)

The numerical method used in this study takes into account the effect of progressive fracturing which the analytical method does not consider. FRACOD does not incorporate Eq. (13.7) in its formulation. Rather, it is based on fundamental solid

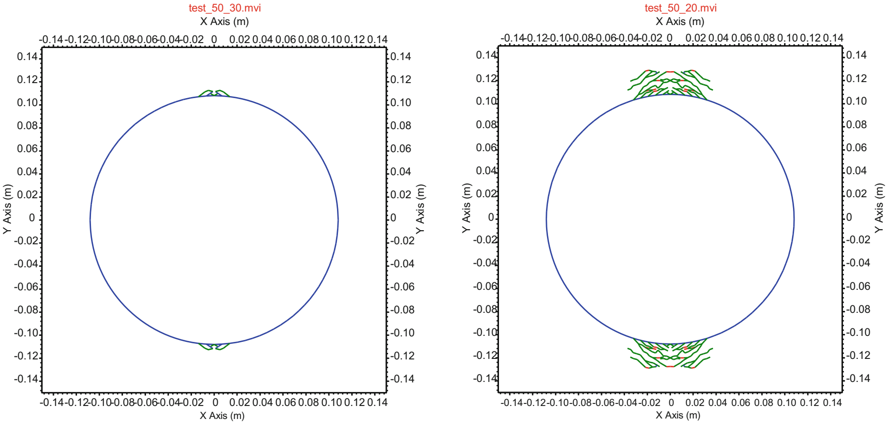

(a) σ_{Hmax} = 50 MPa, σ_{hmin} = 30 MPa (b) σ_{Hmax} = 50 MPa, σ_{hmin} = 20 MPa

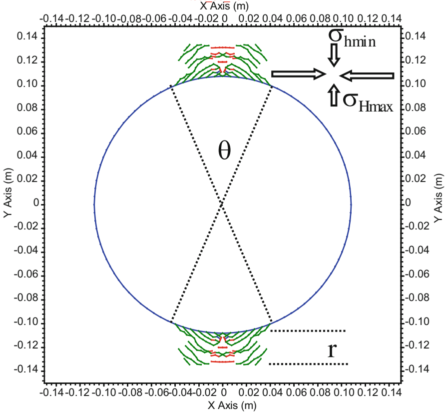

(c) σ_{Hmax} = 50 MPa, σ_{hmin} = 10 MPa

Fig. 13.10 Predicted borehole breakouts at $\sigma_{Hmax} = 50$ MPa and different σ_{hmin}. The definition of the breakout angle (θ) and depth (r_d) is also shown

mechanics and fracture mechanics principles. The numerically predicted breakout angles are plotted against the stress / strength factor in the left side of Eq. (13.7), and they are compared with the analytical results, see Fig. 13.11. The numerical results agree well with the analytical results, suggesting that the breakout angle is not significantly affected by the fracturing process. Rather it is dominated by the initial stress distribution at the borehole wall.

13.4.2.4 Correlations Between Stress/Strength Ratio and Breakout Depth

The normalised depth of the breakout (breakout depth / borehole radius) is found to have a reasonable correlation with the ratio of maximum tangential stress at the

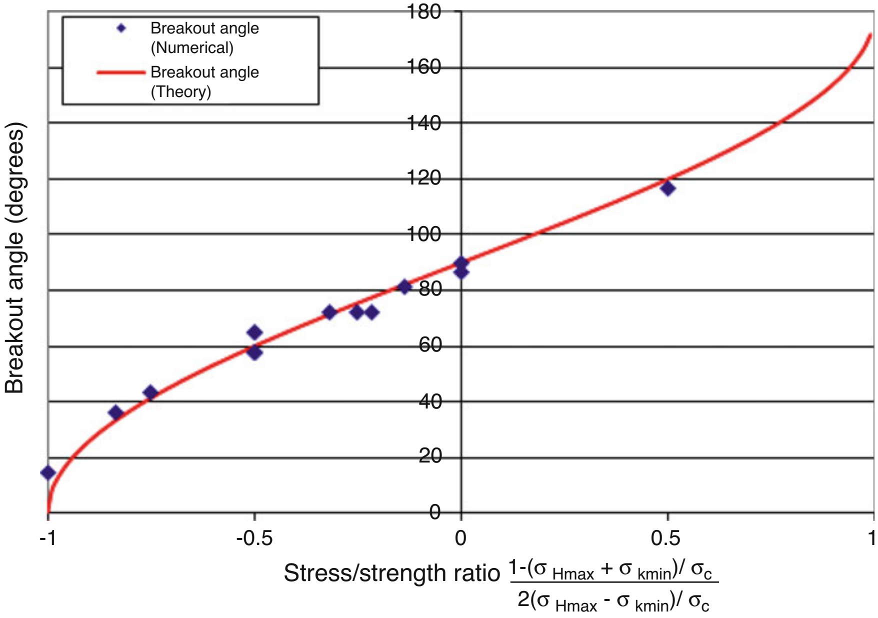

Fig. 13.11 Predicted relationship between stress / strength ratio and the breakout angle

borehole and the rock uniaxial compressive strength, see Fig. 13.12. However, there are noticeable variations in the numerical results from the average correlation curve (Fig. 13.12), possibly due to the limitations in the control of the numerical accuracy and the variation due to the randomness of fracture initiation and propagation. To take into account the variations, we consider the average as well as the upper and lower limits of the stress ratio / breakout depth relationship, as given in Eq. (13.8).

$$(3\sigma_{H\max} - \sigma_{h\min})/\sigma_c = 1 + A\left[\frac{r_d}{r}\right]^B \tag{13.8}$$

where:

r_d = depth of breakouts measured from the original borehole wall
r = original radius of the wellbore.
r_d/r = “normalised breakout depth”.
A, B = the regression parameters to define the three curves in Fig. 13.12. Their values are: A = 15.2, B = 2.67 (Average curve); A = 21.2, B = 3.33 (Upper limit curve); A = 12.6, B = 2.22 (Lower limit curve), respectively.

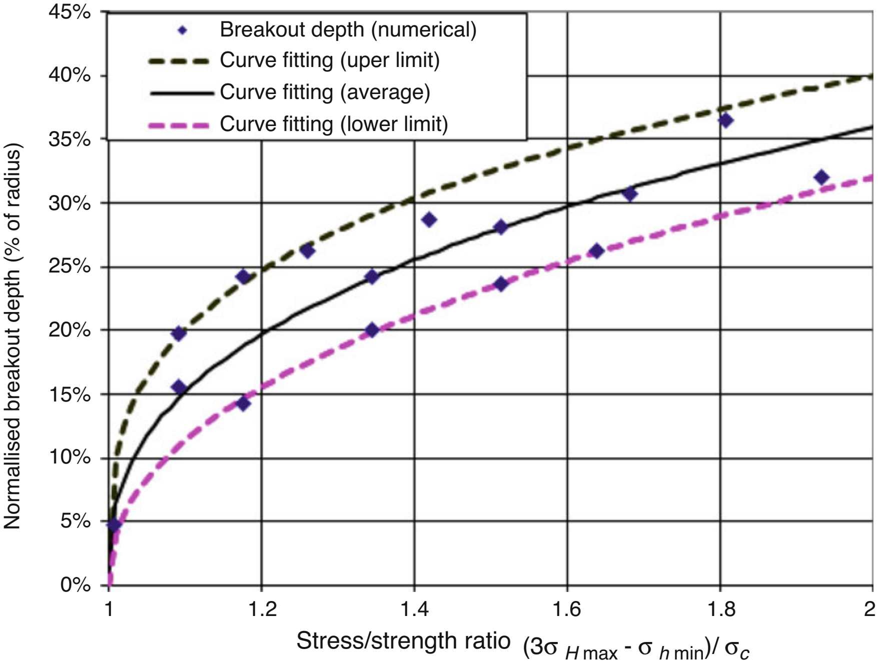

Figure 13.12 Predicted relationship between stress / strength ratio and the normalised breakout depths

13.4.2.5 Back-Analysis of the Magnitude of Principal Horizontal Stresses

When the breakout angle and depth are known, the magnitude of the major and minor horizontal principal stresses can be obtained by solving the systematic equations defined by Eqs. (13.7) and (13.8).

$$\sigma_{H\max} = \frac{1 + (1 - 2\cos(\theta))\left(1 + A\left[\frac{r_d}{r}\right]^B\right)}{4(1 - \cos(\theta))}\sigma_c \tag{13.9}$$

$$\sigma_{h\min} = 3\sigma_{H\max} - \left(1 + A\left[\frac{r_d}{r}\right]^B\right)\sigma_c \tag{13.10}$$

The above equations can then be used to calculate the magnitude of the horizontal stresses in the Habanero No. 1 granite, using the measured breakout dimensions. For each cross section, three stress states will be given: the average, higher, and lower stress state. The uncertainty of the estimated stress state is taken into account by the lower and upper limit values.

13.4.2.6 Stress State in the Habanero No. 1 Granite

The geophysical logging data were used to extract the breakout angle and depth in a number of locations along the wellbore in the granite section. The selected locations are those considered to have a representative borehole breakout angle and depth for a considerable length of the wellbore. In this study, a total of thirteen cross sections were selected to back-analyse the stress states. Table 13.4 lists the measured breakout dimensions of all thirteen cross sections.

After obtaining the breakout angle and depth, Eq. (13.9) and (13.10) were used to calculate the magnitude of the horizontal stresses. Note that the calculated stresses are the effective stresses. To calculate the total stresses, it was assumed that the pore pressure in granite is equal to the mud pressure equivalent to a mud density of 1800 kg/m^3 which was used during drilling below the depth of 4135 m. This gives a mud pressure of 74.1 MPa at the depth of 4209 m.

For each case, the average value, upper and lower limits are given to consider the uncertainty. The predicted horizontal stresses are plotted in Fig. 13.13. The predicted stress variation with depth and the stress ratios are given below. Note that all the back-analysed stresses presented thereafter are total stresses, i.e. the sum of the effective stress and the pore pressure = mud pressure. The vertical stress was estimated based on the study results by Hill et al. (1997) in this area for the sediments, plus a density of 2670 kg/m^3 for the granite.

$$\sigma_{\mathrm{Hmax}}(\mathrm{total}) = (0.033 \sim 0.034) \cdot \mathrm{D}$$

$$\sigma_{\mathrm{hmin}}(\mathrm{total}) = (0.028 \sim 0.032) \cdot \mathrm{D}$$

$$\sigma_{\mathrm{v}}\ (\mathrm{total}) = 0.023 \cdot \mathrm{D}$$

$$\sigma_{\mathrm{Hmax}}/\sigma_{\mathrm{hmin}}/\sigma_{\mathrm{v}}\ (\mathrm{total}) = (1.43 \sim 1.48)/(1.22 \sim 1.39)/1.00$$

where D is the depth in metres.

Table 13.4 Measured borehole breakout dimensions at different depths

Depth (m)	Breakout angle (°)	Normalised breakout depth (r_d/r)
3728	67	6%
3743	61.7	8%
3776	72	13%
3810	61	9%
3885	66.8	14%
3923	61.7	18%
3968	61.7	24%
3996	66.9	17%
4033	61.7	18%
4109	61.7	18%
4121	72	22%
4142	72	15%

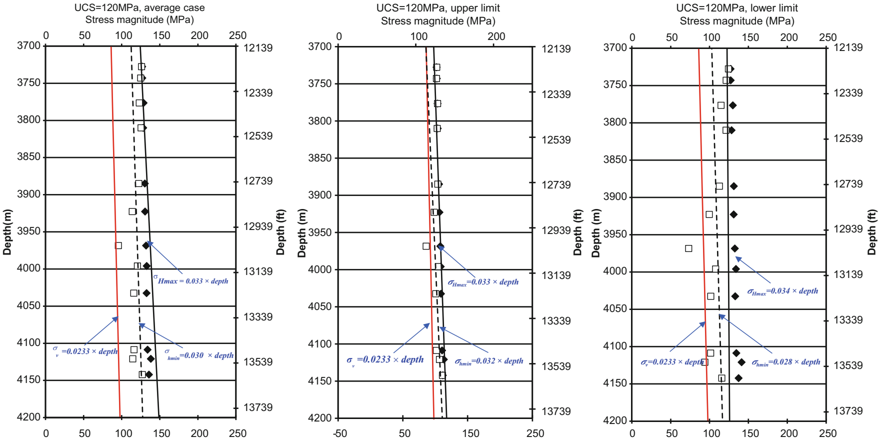

Fig. 13.13 Predicted in situ stress state in granite of Habanero#1 well

This study demonstrates that it is feasible to use the borehole breakout dimension to estimate the magnitude of in situ stress if proper models are used that capture the real breakout mechanisms. The results, however, are sensitive to a number of parameters such as rock strength, fracture properties, etc. This method may only give us a likely range of the in situ stress magnitude rather than a definite value as often obtained from the hydraulic fracturing.

13.4.3 Application to Pohang Geothermal Site, Korea

Kim et al. (2017) presented a regional case study of integrated in situ stress estimation by hydraulic fracturing and analysis of borehole breakout and drilling-induced fractures of EXP-1 well in Pohang, Korea. The vertical borehole EXP-1 has a depth of 1002 m and is used for an initial investigation for the Pohang EGS project. The logs obtained by the borehole televiewer at EXP-1 borehole showed that borehole breakouts occurred at depths between 670 m and 700 m.

Different from the previous example of Cooper Basin EGS site, the hydraulic fracturing operated on EXP-1 borehole already provided the estimation of stress orientation and magnitudes for Pohang geothermal site. In this study, the FRACOD modelling of borehole breakout is a part of integrated strategies for constraining and validating the stress model and eventually produces a best-estimate stress model (Stephansson and Zang 2012).

Table 13.5 Mechanical properties used for modelling EXP-1 borehole breakout

Mechanical properties[a]	
Intact rock strength:	
Young's modulus	50 GPa
Poisson's ratio	0.2
Cohesion	27.4 MPa
Friction angle	34°
Uniaxial compression strength (σ_c)	80 MPa
Fracture toughness:	
Mode I toughness	1 MPa $m^{1/2}$
Mode II toughness	2 MPa $m^{1/2}$
Joint / fracture properties:	
Normal stiffness Kn	50,000 GPa/m
Shear stiffness Ks	12,550 GPa/m
Friction	25.5°
Cohesion	0
Dilation angle	1°

[a] Properties used may vary depending on the depth of core sample

The input parameters used in the numerical analysis (Table 13.5) were mainly from the mechanical properties obtained by conducting laboratory tests on the core samples of EXP-1 borehole. It should be noticed that the measured properties may vary depending on the depth of the core sample. Since the laboratory test for the fracture toughness was not performed, it was assumed that Mode I and Mode II toughness was 1 and 2 MPa $m^{1/2}$, respectively, based on the measurement in similar rock types (Backers and Stephansson 2015).

The minimum horizontal stress, σ_{hmin}, was obtained from measurements of hydraulic fracturing, and numerical analysis was conducted for the range of the maximum horizontal stress ratios (σ_{Hmax} /σ_v). The simulations aimed to determine the horizontal stresses, producing borehole breakouts that were most similar to the real observations from the televiewer logs in the borehole.

Four distinct cross sections at different depths were selected to perform FRACOD simulation and then compare the modeling results with the breakout observations (Fig. 13.14). The breakout angles were almost consistent with the observations from the televiewer. There were differences between the numerical results and the actual observations at the relatively deeper breakout sections. The range of the maximum horizontal stress ratio to vertical stress ((σ_{hmin} /σ_v) was confirmed as 1.3 to 1.4.

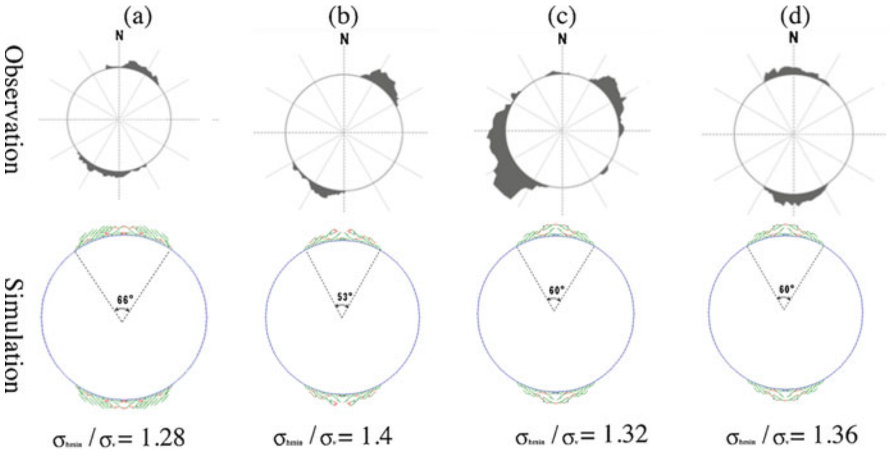

Fig. 13.14 Results of FRACOD simulation. The presented stress ratios correspond to those give the best similarity with the observed breakout geometries at a given depth section in EXP-1 borehole: (**a**) 671–676 m; (b) 684–685 m; (**c**) 694–696 m; and (**d**) 698–699 m

13.5 Concluding Remark

Deep geothermal energy is an attractive option due to its abundant potential and its ability to provide base load power. However, there are grand challenges ahead including efficient drilling, borehole stability, reservoir characterization, advanced downhole monitoring, sustainable production and induced seismicity to name a few. Numerical modeling can be an effective tool to assist in more efficient and sustainable extraction of geothermal heat. Despite the advances achieved for numerical modeling, significant improvement is necessary in order to elevate the current level of understanding in deep geothermal to an industrial one. Following a brief introduction to deep geothermal energy, we presented state of the art of numerical modelling for geothermal energy and two cases concerning convective heat transfer through a single fracture and borehole breakout at geothermal wells. The breakout geometry was used to estimate the in situ stress at the geothermal sites in Cooper Basin, Australia, and Pohang, South Korea. In these applications, numerical modeling was able to mimic the convective heat flow in fractured rock and well bore breakage observed in deep geothermal wells.

Acknowledgements This work was partially supported by the New and Renewable Energy Technology Development Program of the Korea Institute of Energy Technology Evaluation and Planning (KETEP) through a grant funded by the Korean Government's Ministry of Trade, Industry & Energy (No. 20123010110010).

References

Backers T, Stephansson O (2015) ISRM suggested method for the determination of mode II fracture toughness. In: The ISRM suggested methods for rock characterization, testing and monitoring: 2007–2014. Springer, Cham

Bai B, He Y, Li X, Hu S, Huang X, Li J, Zhu J (2016) Local heat transfer characteristics of water flowing through a single fracture within a cylindrical granite specimen. Environ Earth Sci 75 (22):1460

Beckman WA, Broman L, Fiksel A, Klein SA, Lindberg E, Schuler M, Thornton J (1994) TRNSYS the most complete solar energy system modeling and simulation software. Renew Energy 5 (1–4):486–488

Bertani R (2016) Geothermal power generation in the world 2010–2014 update report. Geothermics 60:31–43

Blöcher MG, Zimmermann G, Moeck I, Brandt W, Hassanzadegan A, Magri F (2010) 3D numerical modeling of hydrothermal processes during the lifetime of a deep geothermal reservoir. Geofluids 10(3):406–421

Breede K, Dzebisashvili K, Liu X, Falcone G (2013) A systematic review of enhanced (or engineered) geothermal systems: past, present and future. Geotherm Energy 1(1):1–27

Cacace M, Jacquey AB (2017) Flexible parallel implicit modelling of coupled thermal–hydraulic–mechanical processes in fractured rocks. Solid Earth 8(5):921–941

Cacace M, Blöcher G, Watanabe N, Moeck I, Börsing N, Scheck-Wenderoth M et al (2013) Modelling of fractured carbonate reservoirs: outline of a novel technique via a case study from the Molasse Basin, southern Bavaria, Germany. Environ Earth Sci 70(8):3585–3602

Charlez P, Lemonnier P, Ruffet C, Boutéca MJ, Tan C (1996) Thermally induced fracturing: analysis of a field case in North Sea. In: European Petroleum Conference. Society of Petroleum Engineers, Richardson

Cleary MP (1994) Critical issues in hydraulic fracturing of high-permeability reservoirs. In: European production operations conference and exhibition. Society of Petroleum Engineers, Dallas

Comsol Multiphysics®. ver 5.4. (2018). Reference manual

Diersch HJG (2013) FEFLOW: finite element modeling of flow, mass and heat transport in porous and fractured media. Springer, Berlin

DiPippo R (2012) Geothermal power plants: principles, applications, case studies and environmental impact. Butterworth-Heinemann, Amsterdam, pp 1–17

Economides MJ, Nolte KG (2000) Reservoir stimulation, 3rd edn. Wiley, New York. 856 pp

FRACOM. (2002). User's manual. FRACOM Ltd

Freymark J, Sippel J, Scheck-Wenderoth M, Bär K, Stiller M, Fritsche J-G, Kracht M (2017) The deep thermal field of the upper Rhine Graben. Tectonophysics 694:114–129

Frick S, Kaltschmitt M, Schröder G (2010) Life cycle assessment of geothermal binary power plants using enhanced low-temperature reservoirs. Energy 35(5):2281–2294

Gaston D, Newman C, Hansen G, Lebrun-Grandié D (2009) MOOSE: a parallel computational framework for coupled systems of nonlinear equations. Nucl Eng Des 239(10):1768–1778

Guéguen Y, Boutéca M (eds.) (2004) Mechanics of fluid-saturated rocks (vol 89). Elsevier

Häring MO, Schanz U, Ladner F, Dyer BC (2008) Characterisation of the Basel 1 enhanced geothermal system. Geothermics 37:469–495

He Y, Bai B, Hu S, Li X (2016) Effects of surface roughness on the heat transfer characteristics of water flow through a single granite fracture. Comput Geotech 80:312–321

Hill RR, Meyer JJ, Magee ME (1997). The contemporary stress field of the Nappamerri Trough and its implications for tight gas resources. Report of Department of Geology and Geophysics, University of Adelaide, SA 5005, Australia

Hofmann H, Babadagli T, Zimmermann G (2014a) Hot water generation for oil sands processing from enhanced geothermal systems: process simulation for different hydraulic fracturing scenarios. Appl Energy 113:524–547

Hofmann H, Weides S, Babadagli T, Zimmermann G, Moeck I, Majorowicz J, Unsworth M (2014b) Potential for enhanced geothermal systems in Alberta, Canada. Energy 69:578–591

Huang X, Zhu J, Li J, Bai B, Zhang G (2016) Fluid friction and heat transfer through a single rough fracture in granitic rock under confining pressure. Int Commun Heat Mass Transfer 1 (1):111–123

Itasca (2008) PFC2D (particle flow code in 2 dimensions) theory and background. Minnesota, USA

Kim H, Xie L, Min KB, Bae S, Stephansson O (2017) Integrated in situ stress estimation by hydraulic fracturing, borehole observations and numerical analysis at the EXP-1 borehole in Pohang, Korea. Rock Mech Rock Eng 50(12):3141–3155

Klein SA, (1976) TRNSYS-A transient simulation program. ASHRAE Trans, 82, 623

Kolditz O, Shao H, Wang W, Bauer S (eds) (2015) Thermo-hydro-mechanical-chemical processes in fractured porous media: modelling and benchmarking – closed form solutions, Terrestrial Environmental Sciences, vol 1. Springer, Cham, p 315

Kranz S, Frick S (2013) Efficient cooling energy supply with aquifer thermal energy storages. Appl Energy 109:321–327

Luo F, Rui-Na Xu R-N, Pei-Xue Jiang P-X (2014) Numerical investigation of fluid flow and heat transfer in a doublet enhanced geothermal system with CO2 as the working fluid (CO2-EGS). Energy 64:307–322

Martin CD, Read RS, Martino JB (1997) Observations of brittle failure around circular test tunnel. Int J Rock Mech Min Sci 34(77):1065–1073

MFRAC (2011) User's guide Meyer fracturing simulators, 9th edn. Meyer & Associates, Natrona Heights

MIT (2006) The future of geothermal energy: impact of enhanced geothermal systems (EGS) on the United States in the 21st century. Massachusetts Institute of Technology, Cambridge, pp 1-1–1-34

Olasolo P, Juárez M, Morales M, Liarte I (2016) Enhanced geothermal systems (EGS): a review. Renew Sust Energ Rev 56:133–144

Parkhurst DL, Appelo CAJ (2013) Description of input and examples for PHREEQC version 3—a computer program for speciation, batch-reaction, one-dimensional transport, and inverse geochemical calculations: U.S. geological survey techniques and methods, book 6, chap. A43, 497 p., available only at https://pubs.usgs.gov/tm/06/a43/

Portier S, Vuataz F-D, Nami P, Sanjuan B, Gérard A (2009) Chemical stimulation techniques for geothermal wells: experiments on the three-well EGS system at Soultz-sous-Forêts, France. Geothermics 38:349–359

Potyondy DO, Cundall PA (2004) A bonded-particle model for rock. Int J Rock Mech Min Sci 41:1329–1364

Pruess K (2006) Enhanced geothermal systems (EGS) using CO2 as working fluid — a novel approach for generating renewable energy with simultaneous sequestration of carbon. Geothermics 35:351–367

Regenspurg S, Alawi M, Blöcher G, Börger M, Kranz S, Norden B, Saadat A, Scheytt T, Virchow L, Vieth-Hillebrand A (2018) Impact of drilling mud on chemistry and microbiology of an upper Triassic groundwater after drilling and testing an exploration well for aquifer thermal energy storage in Berlin (Germany). Environ Earth Sci 77:516

Rutqvist J (2011) Status of the TOUGH-FLAC simulator and recent applications related to coupled fluid flow and crustal deformations. Comput Geosci 37:739–750

Rutqvist J, Dobson PF, Garcia J, Hartline C, Jeanne P, Oldenburg CM, Vasco DW, Walters M (2015) The northwest geysers EGS demonstration project, California: pre-stimulation modeling and interpretation of the stimulation. Math Geosci 47:3–2

Scheck-Wenderoth M, Cacace M, Maystrenko Y, Cherubini Y, Noack V, Kaiser B-O, Sippel J, Lewerenz B (2014) Models of heat transport in the central European Basin system: effective mechanisms at different scales. Mar Pet Geol 55:315–331

Shen B, & Stephansson O, (1994) Modification of the G-criterion for crack propagation subjected to compression. Eng Fract Mech, 47(2), 177–189

Shen B (2008) Borehole breakout and in situ stresses. SHIRMS 2008 1:407–418

Shen B, Stephansson O, Rinne M (2002) Simulation of borehole breakouts using FRACOD2D. Oil Gas Sci Technol – Rev, IFP 57(5):579–590

Stephansson O, Zang A (2012) ISRM suggested methods for rock stress estimation – part 5: establishing a model for the in-situ stress at a given site. Rock Mech Rock Eng 45:955–969

Stephansson O, Shen B, Rinne M, Backers T, Koide K, Nakama S, Ishida T, Moro Y, Amemiya K (2003) Geomechanical evaluation and analysis of research shafts and galleries in MIU Project, Japan. In: Proceedings 1st international symposium on underground environment, March, Kyoto, Japan, pp 39–49

Tsang YW (1984) The effect of tortuosity on fluid-flow through a single fracture. Water Resour Res 20(9):1209–1215

Valley B, Evans KF (2007) Stress state at Soultz-sous-Forêts to 5 km depth from wellbore failure and hydraulic observations. In: Proceedings, 32nd workshop on geothermal reservoir engineering, pp 17481–17469

Van der Hoeven M (2013) World energy outlook 2013. Tokyo, International Energy Agency

Vernik L, Zoback MD, Brudy M (1992) Methodology and application of the wellbore breakout analysis in estimating the maximum horizontal stress magnitude in the KTB pilot hole. Sci Drill 3:161–169

Warpinski NR, Moschovidis ZA, Parker CD, Abou-Sayed IS (1994) Comparison study of hydraulic fracturing models - test case: GRI staged field experiment no. 3. SPE Prod Facil 1994:7–16

Watanabe N, Wang W, McDermott C, Taniguchi T, Kolditz O (2010) Uncertainty analysis of thermo-hydro-mechanical coupled processes in heterogeneous porous media. Comput Mech 45 (4):263–280

Watanabe N, Wang W, Taron J, Görke UJ, Kolditz O (2012) Lower dimensional interface elements with local enrichment: application to coupled hydro-mechanical problems in discretely fractured porous media. Int J Numer Methods Eng 90(8):1010–1034

Xu RN, Zhang L, Zhang FZ, Jiang PX (2015) A review on heat transfer and energy conversion in the enhanced geothermal systems with water/CO2 as working fluid. Int J Energy Res 39 (13):1722–1741

Yew CH (1997) Mechanics of hydraulic fracturing. Gulf Professional Publishing

Yoon JS, Zang A, Stephansson O (2014) Numerical investigation on optimized stimulation of intact and naturally fractured deep geothermal reservoirs using hydro-mechanical coupled discrete particles joints model. Geothermics 52:165–184

Yoon JS, Zimmermann G, Zang A (2015a) Discrete element of cyclic rate fluid injection at multiple locations in naturally fractured reservoirs. Int J Rock Mech Min Sci 74:15–23

Yoon JS, Zimmermann G, Zang A (2015b) Numerical investigation on stress shadowing in fluid injection-induced fracture propagation in naturally fractured geothermal reservoirs. Rock Mech Rock Eng 48:1439–1454

Yoon JS, Zimmermann G, Zang A, Stephansson O (2015c) Discrete element modeling of fluid injection-induced seismicity and activation of nearby fault. Can Geotech J 52:1457–1465

Zang A, Stephansson O (2009) Stress field of the Earth's crust. Springer, Dordrecht

Zang A, Yoon JS, Stephansson O, Heidbach O (2013) Fatigue hydraulic fracturing by cyclic reservoir treatment enhances permeability and reduces induced seismicity. Geophys J Int 195 (2):1282–1287

Zang A, Stephansson O, Zimmermann G (2017) Keynote: fatigue hydraulic fracturing. Procedia Eng 191:1126–1134

Zang A, Zimmermann G, Hofmann H, Stephansson O, Min KB, Kim KY (2018) How to reduce fluid-injection-induced seismicity. Rock Mech Rock Eng. https://doi.org/10.1007/s00603-018-1467-4

Zhang Z, Nemcik J, Qiao Q, Geng X (2015) A model for water flow through rock fractures based on friction factor. Rock Mech Rock Eng 48(2):559–571

Zhao ZH (2014) On the heat transfer coefficient between rock fracture walls and flowing fluid. Comput Geotech 59:105–111

Zimmermann G, Reinicke A (2010) Hydraulic stimulation of a deep sandstone reservoir to develop an enhanced geothermal system: laboratory and field experiments. Geothermics 39:70–77
Zimmermann G, Moeck I, Blöcher G (2010) Cyclic waterfrac stimulation to develop an enhanced geothermal system (EGS) – conceptual design and experimental results. Geothermics 39:59–69
Zoback MD, Peska P (1995) In-situ stress and rock strength in the GBRN/DOE pathfinder well South Eugene Island, Gulf of Mexico. J Pet Technol 1995:582–585